

Implementation of the Radiative Transfer Equation on Block-Structured Grids for Modeling Fluorescence Light Propagation in Tissue with Arbitrary Shape

Ludguier D. Montejo ^{a,*}, Alexander D. Klose ^{b,*}, Andreas H. Hielscher ^{a,b}

^a Department of Biomedical Engineering, Columbia University, New York, NY 10027

^b Department of Radiology, Columbia University, New York, NY 10027

ABSTRACT

We developed a method for solving the fluorescence equation of radiative transfer in the frequency domain on block-structured grids. In this way fluorescence light propagation in arbitrarily shaped tissue can be modeled with high accuracy without compromising on the convergence speed of these codes. The block-structure grid generator is developed as a multi-purpose tool that can be used with many numerical schemes. We present results from numerical studies that show that it is possible to resolve curved boundaries with grids that maintain much of the intrinsic structure of Cartesian grids. The natural ordering of this grid allows for simplified algorithms. In simulation studies we found that we can reduce the error in boundary fluence by a factor of five by using a two-level block structured grid. The increase in computational cost is only two-fold. We compare benchmark solutions to results with various levels of refinement, boundary conditions, and different geometries.

Keywords: Block-structured grids, adaptive mesh refinement, equation of radiative transfer, fluorescence tomography

1. INTRODUCTION

The equation of radiative transfer (ERT) has been shown to be the most accurate model for photon propagation in highly absorbing and optically thin media with void-like inclusions. It is therefore the basic equation for fluorescence light and is the most accurate model for reconstruction of the spatial distribution of fluorescent sources in biological tissue. Using the ERT, however, is computationally very expensive.

The ERT can be solved in steady state domain, frequency domain, and time domain.¹ Time domain systems typically pose the most difficulty from an experimental point of view. The steady state domain problem has been shown to be highly ill posed and thus of limited use. The frequency-domain system has thus far been shown to be best for optical tomography.⁴

The frequency domain ERT has received much attention over the past decade.^{1,7,15,16,17} Often, the numerical schemes used to solve the ERT include a combination of discrete ordinates for the angular variable and either a finite differences, finite volume, or finite element method for the spatial variable.^{1,12,3,7,10,11,16,17} The most common type of differencing scheme for the spatial variable is the step method. The step method is a first order scheme and requires a finely discretized grid. In practice, the resolution of the grid is allowed to be coarser than ideal in order to reduce computation time. This compromise introduces discretization errors. Furthermore, the coarse Cartesian grid might not be able to accurately resolve the true physical boundary. This mismatch leads to further errors. The focus of this work is reducing the error due to the boundary mismatch by adaptively refining the coarse Cartesian grid in places where the numerical boundary cannot accurately resolve the physical boundary.

Adaptive mesh refinement algorithms (AMR) have been commonly used in the field of computational fluid dynamics, often implementing finite element methods.⁵ The ERT has been solved using AMR algorithms.¹¹ The ERT in its gray radiation version has also been solved on block-structured grids, a less general version of AMR, by Howell.¹⁰ In this paper we seek to solve the frequency domain ERT using an AMR method that is more specific to the fluorescence tomography problem but is fundamentally inspired by the works cited above.

In general, single coarse grids often cannot accurately resolve curved boundaries. The difference in physical and

* ldm2106@columbia.edu, phone 1 212 854-2320 (L.D. Montejo); ak2083@columbia.edu, phone 1 212 854-5868 (A.D. Klose)

grid boundaries that arise from coarse grids can lead to large numerical errors. In this work we present an algorithm that uses structured Cartesian grids of varying refinement to accurately represent the physical boundary. Fine discretization is only used near boundaries and coarse discretization far from boundaries. We aim to reduce the error due to the mismatch between the numerical and physical boundaries.

This paper is organized as follows. In Section 2 we discuss the development of the block-structured mesh generator. We then present the set of governing transport equations for fluorescence tomography. We conclude the section by presenting the discretization of the transport equations. In Section 3 we present initial numerical results using a 2 level block-structured grid on geometries with curved and non-curved boundaries.

2. METHODS

2.1. Block Structured Grid Generator

Unstructured mesh methods are often used when it is necessary to have the numerical mesh accurately resolve the boundary of the object being studied. While these methods can accurately define most complex boundaries, they are more difficult to code and they are in general slower than structured grid methods. Structured grid methods are faster than unstructured methods because the structure of the neighborhood around a mesh point is known without effort. We have chosen to develop an adaptive method that can resolve complex boundaries to any given level of refinement by placing successively finer mesh points between the numerical boundary defined by the coarsest grid and the boundary defined by the geometry of the object. The benefit of this method lies in retaining much of the ordered nature of structured Cartesian grids.

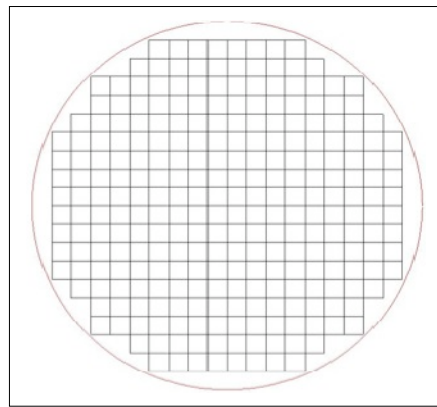


Figure 1: Typical coarse grid

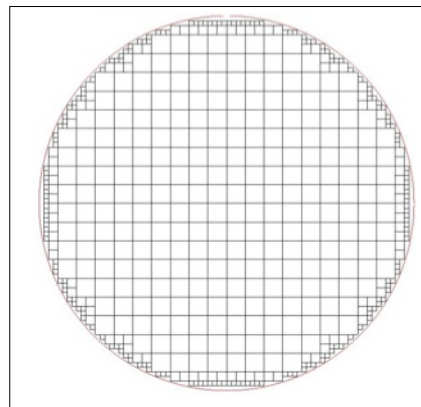


Figure 2: 3-level block structured grid

Our block structured grid generator adaptively refines the computational grid near boundaries that are not well resolved by the overlaying coarse grid. We assume the overlaying coarse grid is sufficiently fine to yield accurate results on the interior of our host medium or that for computational considerations we are not willing to further refine the interior grid. A typical coarse discretization of a 2cm x 2cm cross section is shown in Figure 1. The true geometry is a disk, and the mismatch between numerical and geometrical boundaries is evident. A 3-level, adaptively refined block structured grid fitted to the same cross section is shown in Figure 2. The block-structured grid resolved the physical boundary significantly more than the coarse grid. We implement a 2:1 discretization ratio between the coarse and fine grid. The input to the grid generator code is the boundary information, number of grid levels, and the spatial discretization of the finest grid.

The block-structured grid is an input to the numerical solver. The solver is constructed such that all numerical steps take into account the grid level and location of each point. For a node of level i , the spatial discretization (dx_i , dy_i , dz_i), location of neighbors, and numerical scheme are determined by the solver. The output of the mesh generator is a data structure that contains the following information for each mesh point: location (interior, exterior, or on main boundary), grid level, type of fine/coarse boundary.

2.2. Equation of Radiative Transfer in Frequency Domain

In fluorescence imaging systems the fluorophores are excited by external sources at excitation wavelength λ^x and modulation frequency ω_m . The frequency response of the fluorophores to the modulated source gives information about the marker's physical properties. This information can be used to determine the location of fluorescent sources inside the medium. The excitation field is modeled by ERT (1). The fluorophore emission in response to an excitation field is modeled by ERT (3). The fluorophore response is seen at the optical marker's emission wavelength λ^m . The partly reflecting boundary conditions of the excitation and emission fields are given by (2) and (4), respectively.¹

Excitation field

$$\left(\vec{\Omega} \cdot \vec{\nabla} + \mu_t^x(\vec{r}) + \mu_a^{x \rightarrow m}(\vec{r}) + \frac{i\omega_m}{v} \right) \hat{\psi}^x(\vec{r}, \vec{\Omega}, \omega_m) = \mu_s^x(\vec{r}) \int_{4\pi} p(\vec{\Omega} \cdot \vec{\Omega}') \hat{\psi}^x(\vec{r}, \vec{\Omega}', \omega_m) d\Omega' \quad (1)$$

$$\hat{\psi}^x(\vec{r}, \vec{\Omega}, \omega_m) = \hat{S}^x(\vec{r}, \vec{\Omega}, \omega_m) + R(\vec{\Omega}' \cdot \vec{n}) \hat{\psi}^x(\vec{r}, \vec{\Omega}', \omega_m), \quad \vec{\Omega} \cdot \vec{n} < 0 \quad (2)$$

Emission field

$$\left(\vec{\Omega} \cdot \vec{\nabla} + \mu_t^m(\vec{r}) + \frac{i\omega_m}{v} \right) \hat{\psi}^m(\vec{r}, \vec{\Omega}, \omega_m) = \mu_s^m(\vec{r}) \int_{4\pi} p(\vec{\Omega} \cdot \vec{\Omega}') \hat{\psi}^m(\vec{r}, \vec{\Omega}', \omega_m) d\Omega' + \frac{Q(\vec{r}, \omega_m)}{4\pi} \quad (3)$$

$$\hat{\psi}^m(\vec{r}, \vec{\Omega}, \omega_m) = R(\vec{\Omega}' \cdot \vec{n}) \hat{\psi}^m(\vec{r}, \vec{\Omega}', \omega_m), \quad \vec{\Omega} \cdot \vec{n} < 0 \quad (4)$$

We note the source of the *excitation* field, $\hat{S}^x(\vec{r}, \vec{\Omega}, \omega_m)$, is due to a boundary source. The fluorophore governs the source, $Q^x(\vec{r}, \omega_m)$, of the *emission* field. Equation 5 defines the boundary source. The excitation field given by (6) modulates the internal fluorescence source, (7).¹

$$\hat{S}^x(\vec{r}, \vec{\Omega}, \omega_m) = S_0(\vec{r}, \vec{\Omega}) e^{i\omega_m t} \quad (5)$$

$$\hat{\phi}^x(\vec{r}, \omega_m) = \int_{4\pi} \hat{\psi}^x(\vec{r}, \vec{\Omega}, \omega_m) d\Omega \quad (6)$$

$$Q(\vec{r}, \omega_m) = \frac{\eta \mu_a^{x \rightarrow m}(\vec{r}) \hat{\phi}^x(\vec{r}, \omega_m)}{1 + i\omega_m \tau} \quad (7)$$

Definition of variables and corresponding units can be found in Table 1.

Table 1: Definition of variables.¹

	Definition	Units		Definition	Units
Ψ	Radiance	W cm ⁻² sr ⁻¹	\mathbf{r}	Spatial position (vector)	
Ω	Spatial direction		λ^x	Excitation wavelength	nm
$d\Omega$	Solid angle	sr	λ^m	Emission wavelength	nm
ω_m	Modulation frequency	s ⁻¹	ϕ	Fluence	W cm ⁻¹
μ_a	Absorption coefficient	cm ⁻¹	S	Boundary source	W cm ⁻² sr ⁻¹
μ_s	Scattering coefficient	cm ⁻¹	R	Reflectivity	
μ_t	Attenuation coefficient	cm ⁻¹	τ	Lifetime	s
η	Quantum yield		v	Speed of light in medium	cm s ⁻¹

2.3. Discretization of the frequency domain ERT for use on a block-structured grid

We discretize the ERT by using a discrete ordinates method for the angular variable and a finite differences upwind step-method for the spatial variable.^{13,14,1,12} It is important to stress, the Euler step used in discretizing space will be of variable size; the grid to which the current node belongs will determine the step size. Adapting the method described by Klose [1] to block-structured grids we arrive at the discretized frequency domain ERT for fluorescence tomography.

We use the discrete ordinates method to replace the integral in the ERT with the extended *trapezoidal quadrature rule*.³

$$\int_{4\pi} \psi(\vec{r}, \vec{\Omega}) d\Omega = \sum_{k=1}^K \omega_k \psi_k(\vec{r}) \quad (8)$$

Where ω_k are the predetermined quadrature weights for the discrete ordinates $\Omega_k = (\Omega_x, \Omega_y, \Omega_z)_k$.^{13,14,1} For example, we present the discretization for all ordinates when all directional cosines are positive ($\Omega_x > 0, \Omega_y > 0, \Omega_z > 0$).

Excitation field

$$\begin{aligned} \Omega_x \frac{[\psi^x]_{jlk} - [\psi^x]_{(i-1)jlk}}{\Delta x_{ijl}} + \Omega_y \frac{[\psi^x]_{jlk} - [\psi^x]_{(j-1)lk}}{\Delta y_{ijl}} + \Omega_z \frac{[\psi^x]_{jlk} - [\psi^x]_{j(l-1)k}}{\Delta z_{ijl}} + [\mu_t^x + \mu_a^{x \rightarrow m}]_{jl} [\psi^x]_{jlk} + \\ \frac{\omega_m^i}{v} [\psi^x]_{jlk} = [\mu_s^x]_{jl} \sum_{k'}^K \omega_{k'} p_{kk'} [\psi^x]_{jlk'} \end{aligned} \quad (9)$$

Emission field

$$\begin{aligned} \Omega_x \frac{[\psi^m]_{jlk} - [\psi^m]_{(i-1)jlk}}{\Delta x_{ijl}} + \Omega_y \frac{[\psi^m]_{jlk} - [\psi^m]_{(j-1)lk}}{\Delta y_{ijl}} + \Omega_z \frac{[\psi^m]_{jlk} - [\psi^m]_{j(l-1)k}}{\Delta z_{ijl}} + [\mu_t^m]_{jl} [\psi^m]_{jlk} + \\ \frac{\omega_m^i}{v} [\psi^m]_{jlk} = [\mu_s^m]_{jl} \sum_{k'}^K \omega_{k'} p_{kk'} [\psi^m]_{jlk'} + \frac{Q_{ijl}}{4\pi} \end{aligned} \quad (10)$$

The differencing along an axis switches from forward differencing to backward differencing when the sign of a directional cosine becomes negative. This results in 8 possible spatial discretizations - one for each octant of the standard three-dimensional Cartesian coordinate system. We use the Henyey-Greenstein phase function in (9-10),

$$p_{kk'} = \frac{1 - g^2}{4\pi(1 + g^2 - 2g\Omega_k \cdot \Omega_{k'})^{3/2}} \quad (11)$$

The partly reflective boundary conditions are discretized in a similar way.

Excitation field

$$[\psi^x]_{jlk} = S_k + R(\Omega_{k'} \cdot n_{ijl}) [\psi^x]_{jlk} \quad \Omega_k \cdot n_{ijl} < 0 \quad (12)$$

Emission field

$$[\psi^m]_{jlk} = R(\Omega_{k'} \cdot n_{ijl}) [\psi^m]_{jlk} \quad \Omega_k \cdot n_{ijl} < 0 \quad (13)$$

The fluence is defined using the same quadrature rule.

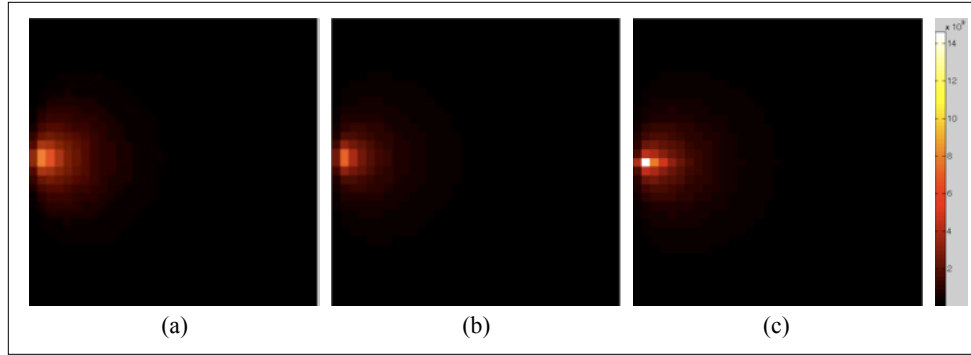


Figure 3: Results for a single boundary source. (a) Results using a fine grid with 65x65 nodes. (b) The results using a 2-level block-structured grid with the coarsest having 33x33 nodes. (c) Results on a coarse grid of 33x33 nodes. All solutions are mapped to the coarsest grid (33x33).

$$\phi_{ijl} = \sum_{k=1}^K \omega_k \psi_{ijkl} \quad (14)$$

3. RESULTS

3.1. Non-curved boundaries

Our first example is a homogeneous, 2cm x 2cm, square medium with one boundary source. To compare various refinement levels we map the fine and block-structured grid solution to the coarsest grid. Figure 3 shows the solution when we use a fine grid, a 2 level grid, and a coarse grid. The 2-level grid has an underlying grid of 33x33 nodes, with refinement points at the boundaries that belong to a grid of 65x65 nodes.

Figure 4 is a plot of the fluence at the boundary for all three grids. Figure 5 is a plot of the error between fine, coarse, and two-level grid solutions at the boundary. At neighborhoods near the source the error between fine and coarse grid solutions ranges from -60% to +40%. The large error near the source occurs because of source position mismatch - the exact source position (defined on the fine grid) does not exist on the coarse grid.

At locations far from the boundary source the error lies between -20% and +20%. This error is a combination of numerical error and error due to poorly resolved boundaries. In contrast, the error between the 2-level block structured and the fine grid solutions is everywhere between 2.5% to 15%. This error is now primarily numerical error. For our sample problem, computation on a two-level grid is more than twice as fast as computation on a fine grid, but also twice slower than computation on a coarse grid (Figure 6). Figure 7 shows the radiance in log scale. Figure 7.b highlights the fine grid refinement at the boundaries and the coarse underlying interior grid.

3.2. Curved boundaries

We investigate the effectiveness of our algorithm on curved boundaries by solving a boundary source problem on a homogeneous disk. The radiance on the entire disk is presented in Figure 8. Furthermore, we assume the exact source position is defined on the fine grid boundary. In general, this means the exact source location does not exist on the coarse grid. This will lead to a mismatch between the true source location (defined on the fine grid) and the approximate location (on the coarse grid).

The fluence at the boundary is presented in Figure 9. The 2-level grid boundary fluence matches the fine grid solution better than the coarse grid. The error between the fine and coarse grid solution is up to 50%. Computing on a fine grid costs up to 5 times more than on a coarse grid. However, computing on a 2 level grid costs only twice more

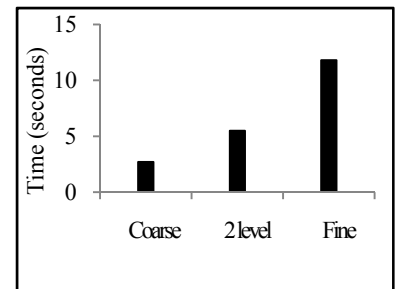


Figure 6: Computational time for a single boundary source on a square.

than computing on a coarse grid. (Figure 10) The error between the fine and 2-level grid solution is between up to 20%. (Figure 11) The three solutions are presented in log scale in order to highlight the boundary refinement used to generate the solution on block-structured grids. (Figure 12)

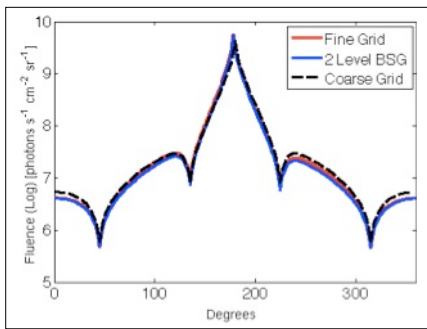


Figure 4: Boundary fluence for 2cm x 2cm square medium. Solid line (red) is the fine grid solution. Blue dashed line is a 2 level BSG solution. Black dashed line is the coarse grid solution.

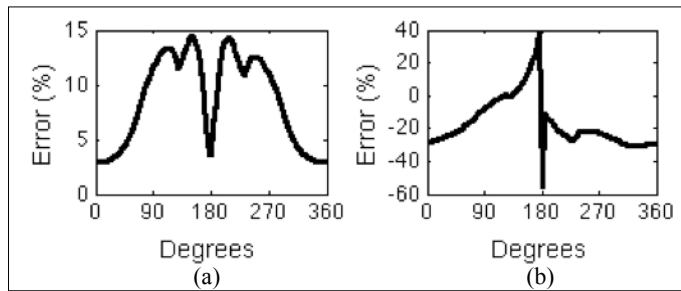


Figure 5: (a) Percent error between fine grid solution and 2-level BSG at the boundary. (b) Percent error between fine grid solution and coarse grid at the boundary.

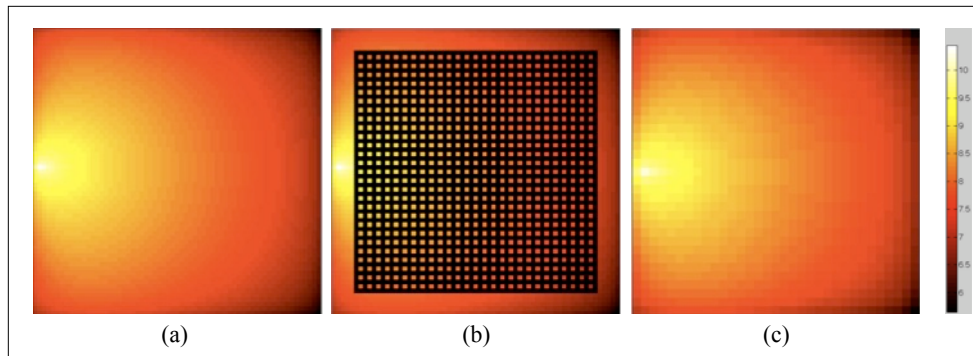


Figure 7: (Log scale) Results for a single boundary source. (a) Fine grid solution with 65x65 nodes. (b) 2-level BSG with solution the coarsest grid a 33x33 grid. (c) Coarse grid solution with 33x33 nodes.

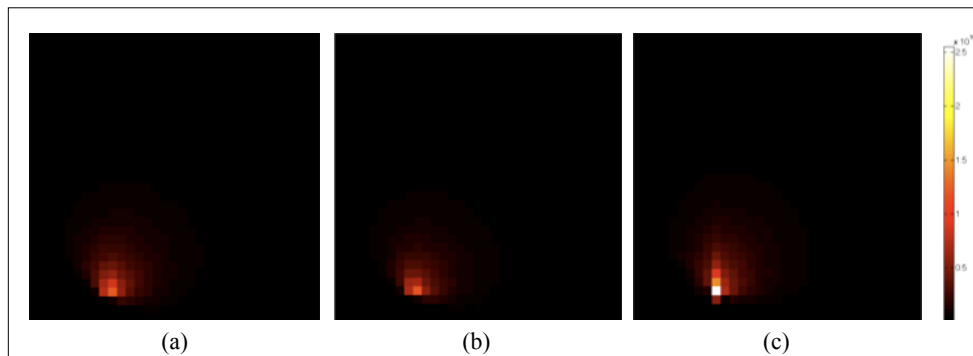


Figure 8: Results for a single boundary source on a disk. (a) Fine grid with 65x65 nodes. (b) 2-level BSG with the coarsest grid a 33x33 grid. (c) Coarse grid of 33x33 nodes. All solutions are mapped to the coarsest grid (33x33).

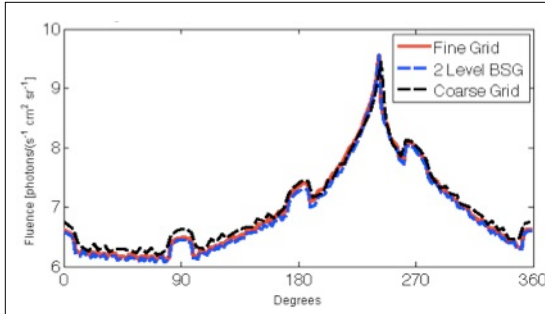


Figure 9: Boundary fluence for 2cm x 2cm square medium. Solid line (red) is the fine grid solution. Blue dashed line is a 2 level BSG solution. Black dashed line is the coarse grid solution.

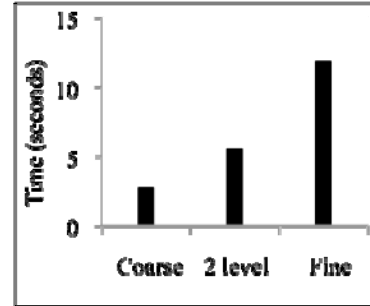


Figure 10: Computational time for a single boundary source on a disk.

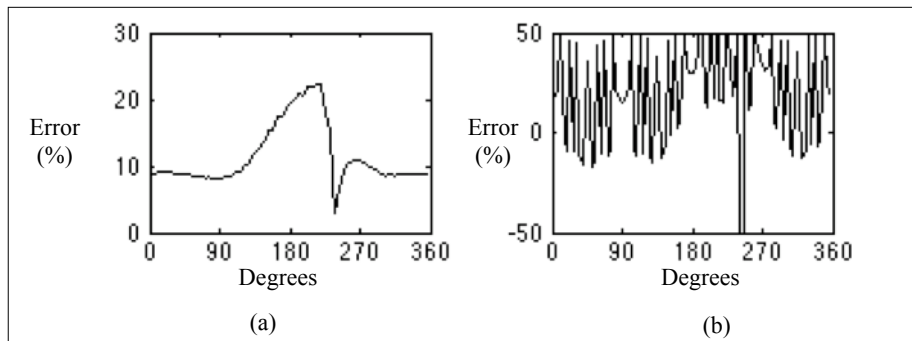


Figure 11: (a) Percent error between fine grid solution and 2-level BSG at the boundary. (b) Percent error between fine grid solution and coarse grid at the boundary.

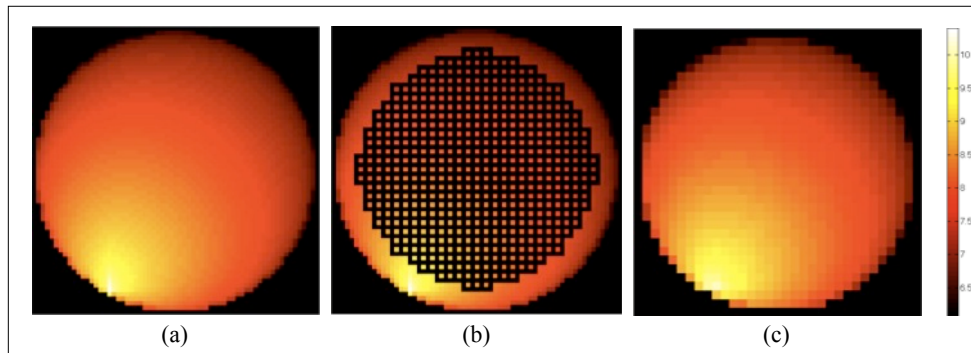


Figure 12: (Log scale) Results for a single boundary source on a disk. (a) Fine grid with 65x65 nodes. (b) 2-level BSG with the coarsest grid a 33x33 grid. (c) Coarse grid of 33x33 nodes.

4. SUMMARY

We have implemented an algorithm for the equation of radiative transfer in frequency domain on block-structured grids. We have showed that it is possible to accurately resolve curved boundaries with Cartesian grids without significantly increasing the number of overall mesh point. Furthermore, we continue to exploit the ordered nature of Cartesian grids by only minimally altering the structure of the algorithm. In addition, we have avoided the increasingly complex algorithms that are necessary when working with other methods that allow for correct representation of physical boundaries (i.e. finite element methods and unstructured finite volume methods).

We implemented a discrete ordinates method to discretize the angular variable and a finite differences scheme for the spatial variable. We have implemented an upwind step method to solve the ERT. Our code allows for increased refinement of the structured Cartesian mesh near boundaries. We have implemented the code for two and three-level grids on geometries with curved and non-curved boundaries. Preliminary results show that we can decrease the error of the solution at the boundary by a factor of five with a two-level grid with a corresponding two-fold increase in computation time. We predict further improvements to the code will allow for better error reduction and a decrease in computation time. Future work will also focus on developing an inverse problem code that uses the present forward model.

5. ACKNOWLEDGEMENTS

The authors would like to thank Dr. Hyun Kim, Dept. of Biomedical Engineering, Columbia University, New York, NY, for many insightful conversations on unstructured mesh implementation. This work was supported in part by two grants from the National Cancer Institute (NCI) at National Institutes of Health (NIH) (5U54CA126513-03: Tumor Microenvironment Network - The role of inflammation and stroma in digestive cancer, Imaging Core, and 4R33CA118666 - Small animal tomography system for green fluorescent protein imaging).

REFERENCES

- [1] Klose, A.D., "Radiative Transfer of Luminescence in Biological Tissue," *Light Scattering Review* **4**, Springer, New York, (2009).
- [2] Klose, A.D., Hielscher, A.H., "Fluorescence tomography with simulated data based on the equation of radiative transfer," *Optics Letters* **28**, No. 12, pp. 1019-1021 (2003).
- [3] Klose, A.D., Hielscher, A.H., "Iterative reconstruction scheme for optical tomography based on the equation of radiative transfer," *Medical Physics* **26** (8), pp. 1698-1707 (1999).
- [4] Hielscher, A.H., "Optical Tomography Imaging of Small Animals," *Current Opinion in Biotechnology* **16**, pp. 79-88 (2005).
- [5] Berger, M.J., Olinger, J., "Adaptive Mesh Refinement for Hyperbolic Partial Differential Equations," *Journal of Computational Physics* **53**, pp. 484-512 (1984).
- [6] Abdoulaev, G.S., Hielscher, A.H., "Three-dimensional optical tomography with the equation of radiative transfer," *Journal of Electronic Imaging* **12** (4), pp. 594-601 (2003).
- [7] Ren, K., Abdoulaev, G.S., Bal, G., Hielscher, A.H., "Algorithm for solving the equation of radiative transfer in the frequency domain," *Optics Letters* **29**, No. 6, pp. 578-280 (2004).
- [8] Russell, W.S., "Polynomial interpolation schemes for internal derivatives distributions on structured grids," *Applied Numerical Mathematics* **17**, pp. 129-171 (1995).
- [9] Atkinson, K.E., [An Introduction to Numerical Analysis, 2nd Edition], John Wiley & Sons, Inc., Canada, (1989).
- [10] Howell, L.H., "A discrete ordinates algorithm for radiation transport using block-structured adaptive mesh refinement," Nuclear Explosives Code Developers' Conference, Monterey, CA., October 21-24, 2002. Approved for public release February 3, (2003).
- [11] Jessee, J.P., Fiveland, W.A., Howell, L.H., Colella, P., Pember, R.B., "An Adaptive Mesh Refinement Algorithm for the Radiative Transport Equation," *Journal of Computational Physics* **139**, pp. 380-398 (1998).
- [12] Klose, A.D., Ntziachristos, V., Hielscher, A.H., "The inverse source problem based on the radiative transfer equation in optical molecular imaging," *Journal of Computational Physics* **202**, pp. 323-345 (2005).
- [13] Case, K.M., Zweifel, P.F., [Linear transport theory], Addison-Wesley, Reading, (1967).
- [14] Duderstadt, J.J., Martin, W.R., [Transport theory], John Wiley, New York, (1979).
- [15] Kim, H.K., Hielscher, A.H., "A PDE-constrained SQP algorithm for optical tomography based on the frequency-domain equation of radiative transfer," *Inverse Problems* **25**, (2009).
- [16] Kim, H.K., Netz, U.J., Beuthan, J., Hielscher, A.H., "Optimal source-modulation frequencies for transport-theory-based optical tomography of small-tissue volumes," *Optics Express* **16**, Issue 22, pp.18082-18101 (2008).
- [17] Gu, X., Ren, K., Hielscher, A.H., "Frequency-domain sensitivity analysis for small imaging domains using the equation of radiative transfer," *Applied Optics* **46** (10), pp. 1624-1632 (2007).